ACS APPLIED MATERIALS & INTERFACES

Research Article

Cite This: ACS Appl. Mater. Interfaces 2019, 11, 24349−24359

www.acsami.org

# Dramatic Enhancement of Optoelectronic Properties of Electrophoretically Deposited $C_{60}$−Graphene Hybrids

Srishti Chugh,[†,‡] Nirmal Adhikari,[§] Ji Hyung Lee,[‡] Diana Berman,[‡] Luis Echegoyen,*[,∥] and Anupama B. Kaul*[,‡,§,⊥]

[†]Department of Metallurgical, Materials and Biomedical Engineering, [§]Department of Electrical Engineering, and [∥]Department of Chemistry, University of Texas at El Paso, El Paso, Texas 79968, United States

[‡]Department of Materials Science and Engineering; PACCAR Technology Institute, and [⊥]Department of Electrical Engineering, University of North Texas, Denton, Texas 76203, United States



**ABSTRACT:** Fullerene ($C_{60}$) and multilayer graphene hybrid devices were fabricated using electrophoretic deposition, where the $C_{60}$ clusters are electrically charged upon the application of an external bias in a polar solvent, acetonitrile, mixed with toluene, which facilitates their deposition on the graphene membranes. Raman spectroscopy unveiled the unique vibrational fingerprints associated with the $A_{2g}$ mode of the $C_{60}$ molecules at ∼1453 $cm^{-1}$, while blue shifts of ∼6 and ∼17 $cm^{-1}$ were also attributed to the G- and 2D-bands of the hybrids relative to bare graphene, suggestive of p-doped graphene. The intensity ratio of the G- and the 2D-bands $I_{2D}/I_G$ (hybrid) dropped to ∼0.18 from ∼0.3 (bare graphene), and this reduction in $I_{2D}/I_G$ is also a signature of hole-doped graphene, consistent with the relatively strong electron accepting nature of $C_{60}$. The electronic conductance of the two-terminal hybrid devices increased relative to bare graphene at room temperature which was attributed to the increased carrier density, and temperature-dependent electronic transport measurements were also conducted from ambient down to ∼5.8 K. Additionally, a low energy shift in the Fermi level, $E_F \approx 140$ meV, was calculated for the hybrids. When the hybrid devices were irradiated with a broadband white light source and a tunable laser source (with a wavelength $\lambda$ ranging from ∼400−1100 nm), a strong photoresponse was evident, in contrast to the bare graphene devices which appeared unresponsive. The responsivity $\mathcal{R}$ of the hybrids was measured to be ∼$10^9$ A/W at $\lambda \approx 400$ nm and ∼298 K, while the detectivity and external quantum efficiency were also exceptional, ∼$10^{15}$ jones and ∼$10^9$%, respectively, at ∼1 V and a light power density of ∼3 mW/$cm^2$. The $\mathcal{R}$ values are ∼10 times higher compared to other hybrid devices derived from graphene reported previously, such as quantum dot-graphene and few-layer $MoS_2$−graphene heterostructures. The strong photoresponse of the $C_{60}$−graphene hybrids reported here is attributed to the doping enhancement arising in graphene upon the adsorption of $C_{60}$. This work demonstrates the exceptional potential of such hybrid nanocarbon-based structures for optoelectronics.

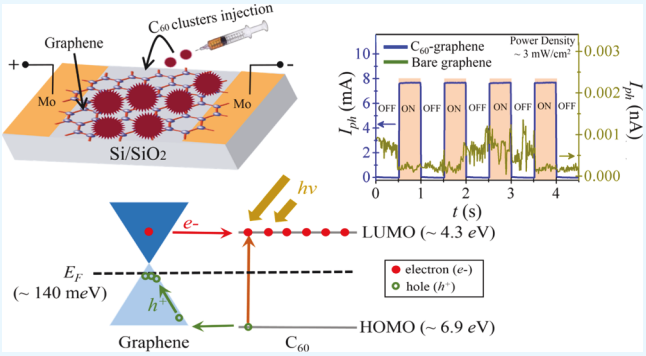


**KEYWORDS:** *$C_{60}$−graphene hybrid device, electrophoretic deposition, Raman spectroscopy, electron transfer, AFM, optoelectronics, photoresponse*

## 1. INTRODUCTION

Two-dimensional (2D) layered materials have emerged as potentially exciting alternatives to Si given their unique properties that are bound to drive advances in electronics and optoelectronics.[1,2] Charge transport mechanisms in these materials[3,4] often differ significantly from conventional, bulk, three-dimensional (3D) semiconductors, which has been another incentive to study the novel aspects of these materials and to propel device innovations. At the same time, conventional 3D semiconductors, particularly compound semiconductors, such as GaAs, InAs, or CdSe, pose challenges from a materials synthesis standpoint, where the complex epitaxial growth process requires an elaborate growth infrastructure, increasing fabrication costs.[5]

Among the family of 2D-layered materials, graphene has played a pivotal role for nanomaterials broadly, fueling the nanotechnology revolution.[6] Graphene exhibits high electron and hole mobility which, under certain conditions, is known to be ballistic; other unique features of graphene include the room temperature $T$ quantum hall effect and a high-charge carrier density, making it exceptionally promising for electronics.[1] In terms of its optical properties, single layer graphene (SLG) absorbs ∼2.3% of the incident light,[7−9] and photodetector devices show a responsivity $\mathcal{R}$ limited to ∼$10^{-3}$ A/W due to a poor light absorption cross-section, short

Received: January 10, 2019
Accepted: May 29, 2019
Published: May 29, 2019




DOI: 10.1021/acsami.9b00603
ACS Appl. Mater. Interfaces 2019, 11, 24349−24359

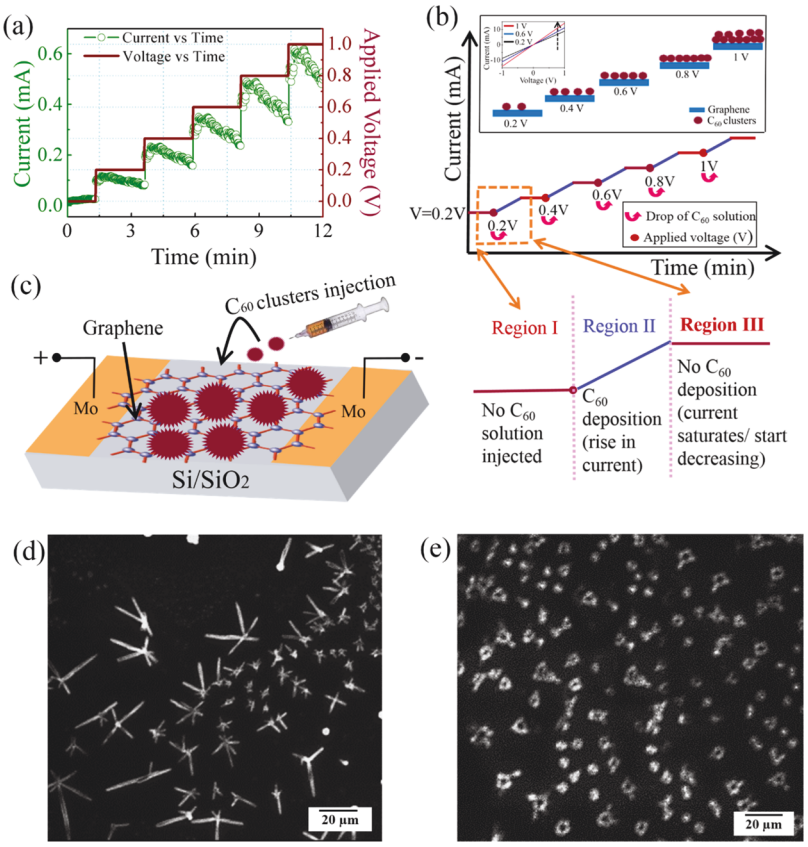


**Figure 1.** (a) $I-t$ and $V-t$ measurements, as $C_{60}$ in toluene−acetonitrile solution is placed on graphene. (b) Illustration of electrophoretic deposition technique (inset shows the deposition of $C_{60}$ clusters as a function of applied voltage during electrophoretic deposition). As the $V$ is increased, the $I$ starts to increase, which leads to more aggregation of $C_{60}$ clusters as represented by the $I-V$ curves. For the same interval of $t$ (∼1.5 min), ∼0.2 V generates less current due to which there was less aggregation of $C_{60}$ clusters on top of the graphene membrane (e.g., region I), whereas for ∼1 V, an increase in $I$ was observed (region II), which implies more aggregation of $C_{60}$ on top of the graphene membrane. When all of the $C_{60}$ is deposited, the current saturates and starts decreasing (region III). (c) Schematic representation of the device (not to scale) and the electrophoretic deposition process where droplets of $C_{60}$ clusters are injected using a syringe onto the graphene membrane and the electrodes on either end represent the areas where the bias voltage is applied during electrophoretic deposition. SEM image of (d) $C_{60}$ clusters deposited when the drop of the suspension solution was injected continuously, which results in asymmetric clusters, and (e) symmetric $C_{60}$ cluster formation when one drop of the suspension solution is injected after every 1.5 min interval of $t$.

photon-generated carrier lifetimes in the picosecond range, and the absence of optical gain.[10] Improvements in the photoresponse of SLG-based photodetectors to improve $\mathcal{R}$ has relied on techniques such as the application of an external vertical bias,[11] fabricating graphene-based hybrids, or heterostructures using transition metal dichalcogenides (TMDCs),[12] quantum dots (QDs),[13] and more recently, integration with methylammonium lead iodide ($MAPbI_3$) perovskites.[14] However, the fabrication process for making these graphene-based photodetectors is relatively complicated and challenging, and the devices also have a slow response time of ∼5 s which prohibits their use in high-speed detectors.[15]

At the same time, several hybrid nanocarbons, such as fullerenes ($C_{60}$)−graphene,[16−18] $C_{60}$−nanoribbons,[19] TMDC−$C_{60}$,[20] $C_{60}$−hexagonal boron nitride,[17,21,22] and superatomic crystals ($C_{60}$ and metal chalcogenides crystals)[23] in various geometric configurations have been prepared using covalent or noncovalent interactions for optoelectronics, photonics, energy storage, and solar cells. Amongst these, the $C_{60}$−graphene hybrid structure has received some attention, in particular for applications such as in lithium-ion batteries, in electrodes for photovoltaics, and in supercapacitors.[24,25] Its importance as an organic thermoelectric material has also emerged recently, where the $\pi-\pi$ stacking of graphene integrated with $C_{60}$ is evident in a liquid−liquid interface using poly(3,4-ethylenedioxythiophene) poly(styrenesulfonate) to enhance the thermal and electrical conductivities of the hybrid.[26] Recently, vertical heterostructures composed of $C_{60}$ thin films on SLG have been assembled and vertical graphene transistors were also fabricated.[27] Experimental and theoretical studies have shown that the adsorption of $C_{60}$ on bare graphene is governed by van der Waals interactions.[16,28] Manna and Pati have demonstrated noncovalent interactions of $C_{60}$ with graphene, which shows $C_{60}$ physisorbed on graphene, and electrons being transferred from graphene to $C_{60}$.[29]

In this work, we propose $C_{60}$−graphene hybrids for photodetector devices, where $C_{60}$ is deposited onto graphene using an electrophoretic deposition technique. The enhanced optoelectronic properties of the hybrid are attributed to charge transport between graphene and $C_{60}$. The $C_{60}$−graphene hybrid relies on the relatively strong electron-accepting characteristics of $C_{60}$ and the good charge transport properties associated with graphene,[27] where this synergistic interaction allows photogenerated carriers to be collected efficiently to enable high-performance, high $\mathcal{R}$ optoelectronic devices for


DOI: 10.1021/acsami.9b00603
ACS Appl. Mater. Interfaces 2019, 11, 24349−24359

detection. Besides the optoelectronic measurements, *T*-dependent Raman spectroscopy provided insights on the origins of a superior optoelectronic device performance, which reveals the hole-doped nature of graphene when it is in contact with $C_{60}$. To the best of our knowledge, this is the first successful demonstration of a $C_{60}$−graphene-based photodetector, where the optoelectronic response was measured across a broad wavelength $\lambda$ range from ∼400−1100 nm using a tunable laser source at room *T*, and the optoelectronic measurements were conducted from room temperature down to $T \approx 5.8$ K. The measured $\mathcal{R}$ of the hybrid nanocarbon-based devices is ∼10 times larger than any previously reported graphene-based hybrid device, while the detectivity *D* and external quantum efficiency (EQE) were equally exceptional, $\sim 10^{15}$ jones and $\sim 10^{9}$%, respectively, at ∼1 V with a light power density of ∼3 mW/cm$^2$. Our work serves as a pivotal stepping-stone for future studies to explore the immense possibilities of $C_{60}$−graphene hybrids for optoelectronics and photodetectors that are essential in defense, surveillance, and imaging-related applications.[30]

## 2. RESULTS AND DISCUSSION

In order to construct our nanodevices, mechanically exfoliated graphene was transferred onto molybdenum (Mo) electrodes using a viscoelastic stamping process described by Saenz et al. for $MoS_2$ membranes.[31] Formulations of $C_{60}$ at concentrations of ∼5, ∼19, ∼35, and ∼45 $\mu$M were made in toluene and acetonitrile solution, at an acetonitrile/toluene concentration of 3:1 (v/v). This technique, first reported by Kamat et al.,[32] showed that the presence of a polar solvent such as acetonitrile charges the $C_{60}$ clusters and facilitates their deposition on the desired surface as they respond to an external electric field during electrophoretic deposition. The clusters of $C_{60}$, thus obtained, are assembled in an orderly fashion.[32] The electrophoretic deposition technique allowed the $C_{60}$ molecules to decorate the graphene surface, without heating the sample. Figure 1a,b show the current−time (*I*−*t*) and voltage−time (*V*−*t*) plots measured for the graphene assembly upon the injection of the $C_{60}$ solution, while Figure 1c conceptually illustrates the electrophoretic deposition process. Initially, a voltage *V* was applied to the Mo contacts and the current *I* was measured in the absence of $C_{60}$ at $V \approx 0.2$ V to calibrate the system. For $V < 0.2$ V, the *I* level was low, as indicated schematically by region I in Figure 1b. Upon injection of the $C_{60}$ solution at $V \approx 0.2$ V, the *I* increased gradually and $C_{60}$ clusters became charged in the presence of acetonitrile and started to deposit on top of the graphene membrane (region II). The inset of Figure 1b of the *I*−*V* characteristic schematically illustrates the $C_{60}$ clusters deposited on graphene at progressively increasing electrophoretic deposition voltages. As the electrophoretic voltage *V* was increased further up to ∼1 V at ∼0.2 V increments with a steady flow of $C_{60}$ solution injected at every step, the *I* peak increased accordingly, as more aggregation occurs through the deposition of the $C_{60}$ clusters. When all the clusters were deposited, the *I* peak starts to decrease with no further $C_{60}$ deposition (region III) because of Joule heating in the channel.

The surface morphology of the $C_{60}$ clusters on the graphene membrane was examined using scanning electron microscopy (SEM), where the micrographs in Figure 1d revealed the asymmetric nature of the $C_{60}$ clusters deposited on the graphene membrane when the solution was injected continuously. The asymmetric clusters were structurally similar to those reported previously,[33] borne out of the liquid−liquid interfacial precipitation method; this shows that the conduction of the hybrid is negligible under these conditions. In order to obtain more symmetric clusters,[32] one drop of the $C_{60}$ suspension was injected after $t \approx 1.5$ min intervals, which resulted in the $C_{60}$ clusters coalescing, as shown in Figure 1e. It is worth noting that the current should be measured continuously during this electrophoretic deposition process to yield a symmetric morphology of the $C_{60}$ clusters, as in Figure 1e. After the electrophoretic deposition was completed, the $C_{60}$−graphene sample was heated at ∼120 °C for ∼5 min to drive-off the residual toluene and acetonitrile solvents. It should be noted that acetonitrile−toluene solution has minimal impact on the electrical conductance of the device because it largely evaporates after annealing at 120 °C.

Optical absorption properties of the $C_{60}$ suspensions were measured using a CARY 5000 spectrophotometer for $C_{60}$ concentrations of ∼5, 19, 3, and 45 $\mu$M, respectively, in the acetonitrile−toluene solution, as shown in Figure 2a. The

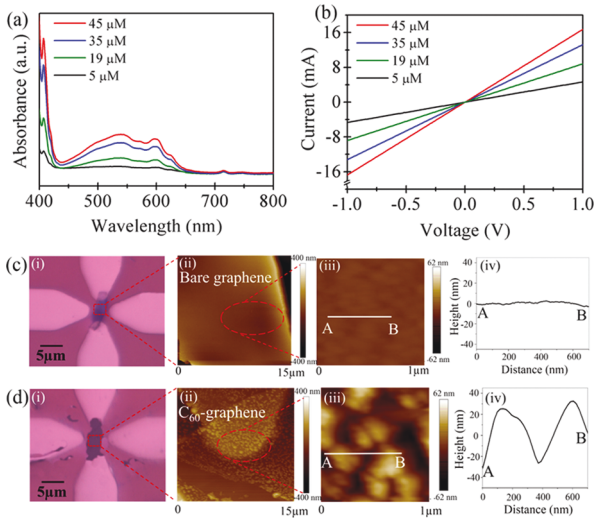


**Figure 2.** (a) Absorbance as a function of $\lambda$ for various concentrations of $C_{60}$ in 3:1 (v/v) acetonitrile/toluene. (b) *I*−*V* characteristics of $C_{60}$−graphene hybrids at various concentrations of $C_{60}$ in 3:1 (v/v) acetonitrile/toluene. [c(i),d(i)] Show optical micrographs of the bare graphene and $C_{60}$−graphene devices, respectively, with the red-dotted square depicting the [c(ii),d(ii)] large-area AFM scan for bare graphene and $C_{60}$−graphene devices, respectively. [c(iii),d(iii)] show the magnified AFM scans from A to B of bare graphene and $C_{60}$−graphene, respectively. [c(iv)] Reveals a smooth graphene surface from the A-to-B scan direction. [d(iv)] The A-to-B scan direction showing clustering of $C_{60}$ on the graphene membrane where the island height profile is ∼25−30 nm and lateral cluster lengths are ∼300−500 nm. In both of the cases considered, the measured thickness of the bare graphene membrane is ∼19 nm.

solutions exhibit a structure-less broad absorption from $\lambda \approx$ 400−700 nm. The principal band of $C_{60}$ at $\lambda \approx 410$ nm is due to being orbitally allowed transitions from the ground state to the excited states,[34] and a broad weak continuum was seen between $\lambda \approx$ 430−640 nm with the maximum at $\lambda \approx 540$ nm. This observation is explained on the basis of the vibronic bands of the electronic transitions from the lowest unoccupied molecular orbital (LUMO) to various multimode degenerate states, including the three-fold degenerate $1T_{1u}$ states.[35] In general, the absorbance of the solution increased as the


DOI: 10.1021/acsami.9b00603
ACS Appl. Mater. Interfaces 2019, 11, 24349−24359

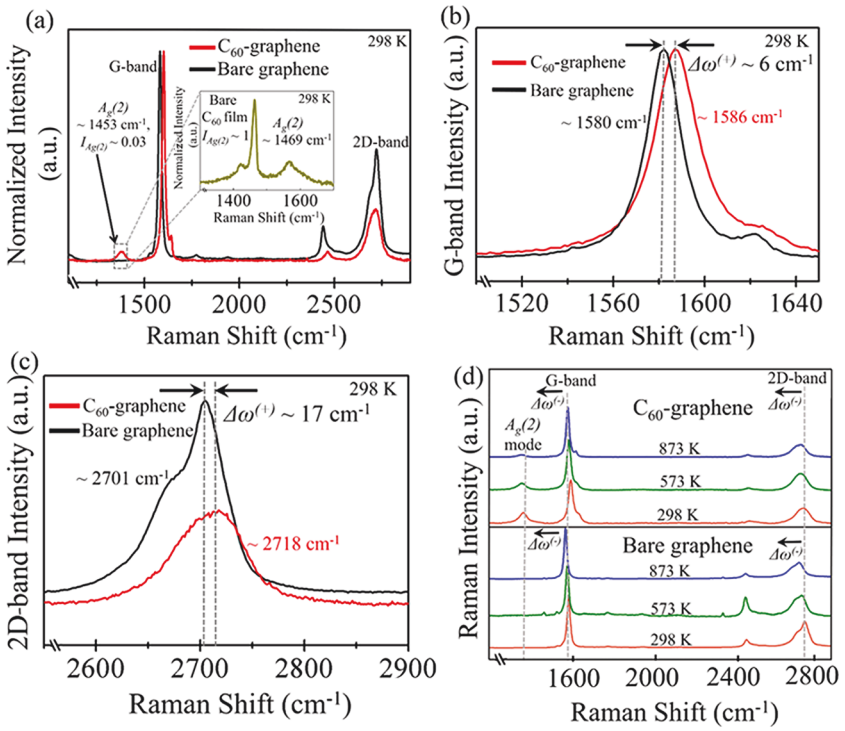


**Figure 3.** (a) Raman spectra of bare graphene and $C_{60}$−graphene at room $T$ (inset shows the Raman spectra of the $C_{60}$ film). The mechanically exfoliated graphene membranes show an intense tangential mode G-band at ∼1580 $cm^{-1}$ and a 2D-band at ∼2701 $cm^{-1}$. Expanded Raman spectra for (b) G-band, and (c) 2D-band. The spectra highlights the $\Delta\omega^{(+)}$ shift of ∼6 $cm^{-1}$ for the G-band and ∼17 $cm^{-1}$ for the 2D-band. (d) Raman spectra of bare graphene and $C_{60}$−graphene with the $\Delta\omega^{(-)}$ shift as $T$ is increased from 298 to 873 K. The intensity ratio of the G- and the 2D-bands of bare graphene and $C_{60}$−graphene are also calculated and are summarized in Table 1.

concentration of $C_{60}$ increased, which is consistent with the Lambert−Beer Law.

The $I$−$V$ measurements shown in Figure 2b reveal a linear increment in current as the concentration of $C_{60}$ in the solution increases, consistent with a higher density of $C_{60}$ on the deposited substrate. Contact-mode atomic force microscopy (AFM) was used to probe the structural morphology of the $C_{60}$ clusters on the graphene surface. The $C_{60}$ concentrations of ∼45 $\mu$M yielded the highest conductance, which was the concentration used for the subsequent experiments and analysis. Figure 2c(i),d(i) depict the optical micrographs of the bare graphene and $C_{60}$−graphene, respectively, where the red dotted square indicates the AFM scan area. The height profile measurements using the AFM were conducted over an area of ∼15 $\mu$m × 15 $\mu$m, as shown in Figure 2c(ii),d(ii), respectively, while the scan area in Figure 2c(iii),d(iii) was ∼1 $\mu$m × 1 $\mu$m. The measurements were conducted at a scan speed of 1 Hz. Roughness profile analysis along the A-to-B scan direction confirms that the bare graphene in Figure 2c(iv) has an ultra-flat surface with no detectable periodicity. Meanwhile, clustering of $C_{60}$ particles on the graphene membrane is observed in Figure 2d(iv); the cluster diameter in the latter was determined to lie in the ∼300−500 nm range, with a height amplitude of ∼25−30 nm.

The devices were further characterized using Raman spectroscopy, where the mechanically exfoliated graphene membranes show an intense tangential mode G-band and 2D-band[36] at ∼1580 and ∼2701 $cm^{-1}$, respectively, as depicted in Figure 3a. Because of the presence of $C_{60}$ on top of the graphene membrane, a new peak at ∼1453 $cm^{-1}$ was observed, and this peak is attributed to the $A_g(2)$ band of $C_{60}$, where the normalized intensity $I_{A_g(2)} \approx 0.03$. This feature arises from the $C_{60}$ molecules, as is evident through a comparison with the bulk bare $C_{60}$ film whose Raman spectra is shown in the inset of Figure 3a, where an intense peak is seen at ∼1469 $cm^{-1}$ with a relatively normalized peak intensity $I_{A_g(2)} \approx 1$. The $A_g(2)$ peak in $C_{60}$ is due to the electron accepting nature of $C_{60}$ giving rise to the $C_{60}$ "pentagonal pinch mode."[16] As is evident from Figure 3a, a red shift $\Delta\omega^{(-)}$ of the $A_g(2)$ mode is seen for the $C_{60}$−graphene hybrid compared to bare $C_{60}$. Additionally, a decrease in $I_{A_g(2)}$ is observed for the hybrid which is attributed to the pentagonal pinch mode of $C_{60}$ where a 100% tangential displacement is seen for the C-atoms in the $C_{60}$ molecule that causes the pentagons to shrink and the hexagons to expand in the presence of graphene, this suggests a strong interaction of the $C_{60}$ cages with the graphene sheets.[37] The additional confirmation of the bonding environment can be gained by additional material characterization techniques such as X-ray photoelectron spectroscopy or X-ray absorption near edge structure for a future study.

Besides the $A_g(2)$ Raman mode, the $C_{60}$−graphene hybrid devices show a blue shift $\Delta\omega^{(+)}$ of ∼6 $cm^{-1}$ for the G-band (increases up to ∼1586 $cm^{-1}$, Figure 3b), and a blue-shift $\Delta\omega^{(+)}$ of ∼17 $cm^{-1}$ is also observed for the 2D-band (increases up to ∼2718 $cm^{-1}$, Figure 3c). Jnawali et al.[16] has investigated $C_{60}$−graphene hybrids using Raman and THz time-domain spectroscopy and demonstrated that $C_{60}$ acts as an electron acceptor, leading to hole-doped graphene. This is consistent with our Raman data in Figure 3b,c taken at $T \approx 298$ K, where the $\Delta\omega^{(+)}$ (blue) shift of the G-band and 2D-band are observed for the $C_{60}$−graphene hybrids, confirming hole doping. As a result of the blue-shift in the G-peak due to hole-doping, the reduction in the Fermi level $E_F$ of graphene


DOI: 10.1021/acsami.9b00603
ACS Appl. Mater. Interfaces 2019, 11, 24349−24359

can be deduced, which we compute later in the discussion. Similarly, Yu et al.[24] showed that electron transfer to $C_{60}$ also influences the intensity of the 2D-mode $I_{2D}$, where the $I_{2D}/I_G$ ratio drops at 298 K as the carrier concentration increases, with the concomitant $\Delta\omega^{(+)}$ shift. The change in intensity ratios are summarized in Table 1 where the $I_{2D}/I_G$ ratio dropped by more than 60% for the hybrids compared to bare graphene at $T \approx 298$ K, and the data for $T > 298$ K are also presented, and discussed next.

**Table 1. Ratio of $I_{2D}/I_G$ as a Function $T$ for Bare Graphene and the $C_{60}$−Graphene Hybrid**[a]

| | $I_{2D}/I_G$ | | |
|---|---|---|---|
| device | 298 K | 573 K | 873 K |
| bare graphene | ∼0.3 | ∼0.26 | ∼0.23 |
| $C_{60}$−graphene | ∼0.18 | ∼0.11 | ∼0.09 |

[a]The ratio in the bare graphene remains largely unchanged as $T$ increases, while the ratio experiences a more significant decrease with $T$ for the hybrid. Additionally, the decrease in the ratio of the hybrid at room temperature compared to the bare graphene is also a signature of hole doping in graphene.

The $T$-dependent Raman spectra from 298 to 873 K of bare graphene are shown in Figure 3d at the bottom, while the top of Figure 3d illustrates the spectra for the $C_{60}$−graphene hybrids. The $C_{60}$−graphene and the bare graphene both show a $\Delta\omega^{(-)}$ shift in the G-band and the 2D-band as $T$ increases, which is related to electron−phonon coupling, as noted previously.[36] The 2D-band is known to be more sensitive to changes in the electronic band structure. Therefore, as $T$ increases, thermally induced strain causes the C−C bonds to stretch, which impacts the electronic band structure alongside the Raman 2D-band position, from which properties such as the thermal-expansion coefficient are deduced.[38] Meanwhile, the G-mode is intimately tied to the optical phonons which are sensitive to the carrier density more so than the $T$-induced strain.[39] The $I_{2D}/I_G$ ratios tabulated as a function of $T$ in Table 1 show that this ratio decreases more significantly with $T$ for the hybrids than for bare graphene, and is likely due to electron transfer from graphene to $C_{60}$.[40]

Elaborating more upon the data in Figure 3d, the $\Delta\omega^{(-)}$ shift in the G-band for the graphene membrane was observed to be ∼12.9 $cm^{-1}$ as $T$ increased from 298 to 873 K, as seen from Figure 4a-bottom. Similarly, the $C_{60}$−graphene hybrid (Figure 4b-top) yielded a $\Delta\omega^{(-)}$ of ∼11.3 $cm^{-1}$ within the same thermal regime for the G-band. Interestingly, the $\Delta\omega^{(-)}$ shift for the 2D-band in Figure 4b was higher in both the $C_{60}$−graphene (∼19.1 $cm^{-1}$) and the bare graphene (∼16.2 $cm^{-1}$) as $T$ increased. Furthermore, the frequency shift resulting from the $T$-dependence of the G- and 2D-band for the $C_{60}$−graphene films was calculated and fit to $\omega = \omega_0 + \chi T$, where $\omega_0$ is the Raman frequency shift when the $T$ is extrapolated to 0 K, and $\chi$ is the first-order $T$-coefficient extracted from the slope of the linear-fit. The extracted absolute value of the G-band $T$-coefficient ($\chi_G$) for $C_{60}$−graphene is shown in Figure 4c, where $\chi_G \approx 0.01618$ $cm^{-1}$ $K^{-1}$; the inset shows the data for bare graphene where $\chi_G$ was calculated to be ∼0.01818 $cm^{-1}$ $K^{-1}$. Similarly, the 2D-band $T$ coefficient ($\chi_{2D}$) for $C_{60}$−graphene was calculated to be ∼0.02156 $cm^{-1}$ $K^{-1}$ in Figure 4d, while the inset shows the data for the bare graphene with $\chi_{2D} \approx$ 0.02366 $cm^{-1}$ $K^{-1}$. The $\chi_G$ and $\chi_{2D}$ values were ∼12.5 and ∼9.7% lower, respectively, for the $C_{60}$−graphene hybrid compared to bare graphene. Additionally, previous investigations have also shown $\chi_G < \chi_{2D}$ which is mostly attributed to the "self-energy" contribution from the G-band and is independent of the thermal expansion.[36]

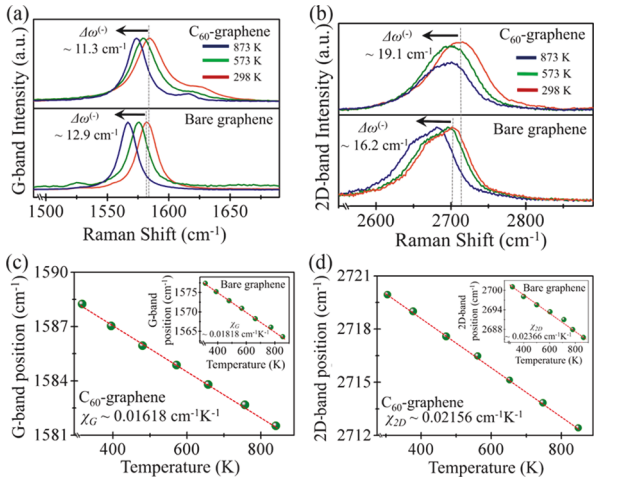


**Figure 4.** Variation of (a) G-band and (b) 2D-band as a function of $T$ in bare graphene and $C_{60}$−graphene (only three $T$'s are shown for ease of representation). Linear fit (dotted red lines) showing the extracted (c) $\chi_G$ for the G-band, and (d) $\chi_{2D}$ for the 2D-band in bare graphene (inset) and $C_{60}$−graphene. The $\chi_G$ and $\chi_{2D}$ values computed for the $C_{60}$−graphene hybrid were: $\chi_G \approx 0.01618$ $cm^{-1}$ $K^{-1}$ and $\chi_{2D} \approx$ 0.02156 $cm^{-1}$ $K^{-1}$, and for bare graphene $\chi_G \approx 0.01818$ $cm^{-1}$ $K^{-1}$ (inset in c) and $\chi_{2D} \approx 0.02366$ $cm^{-1}$ $K^{-1}$ (inset in d). The $\chi_G$ and $\chi_{2D}$ values were ∼12.5 and ∼9.7% lower for the $C_{60}$−graphene hybrid compared to bare graphene.

We then proceeded to conduct two-terminal $I$−$V$ measurements (no external gate voltage applied) of the hybrid structures at room $T$, where the $I$ at ∼1 V was ∼20× higher for the hybrid when compared to the bare graphene, as shown in Figure 5a. Because with $C_{60}$ in direct contact with the graphene membrane, the conduction path includes the $C_{60}$−graphene interface, where the two carbon surfaces are in intimate contact via van der Waals interactions.[14] In our case, the thickness of bare graphene is ∼19 nm observed from AFM shown in Figure 2c. Fang et al.[41] determined that graphene with thicknesses ranging from ∼0.67 to ∼4.4 nm (∼2 to ∼13 layers), the conductivity rapidly decreases with increasing thickness (reduction rate, >20% $nm^{-1}$). The conductivity slowly decreases thereafter and is constant for thicknesses of upto ∼55 nm (165 layers) with a reduction rate <1% $nm^{-1}$.[41] Temperature-dependent electronic transport measurements were also conducted from ∼5.8 to 298 K, as shown by the data in Figure 5b,c. At $V \approx 1$ V, $I$ increases from ∼0.38 mA at ∼5.8 K to ∼0.8 mA at ∼298 K for bare graphene (Figure 5c) and ∼9 mA at ∼5.8 K to ∼20 mA at ∼298 K for the $C_{60}$−graphene hybrid (Figure 5b). Figure 5d shows the $T$-dependence of the resistance ($R$) in greater detail, with the inset illustrating the $R$−$T$ characteristic of bare graphene and the $C_{60}$−graphene hybrid, which depicts the general decrease in $R$ as $T$ is increased.[42] Prior reports also show that $R$ of bare graphene decreases as $T$ increases from ∼5 to 340 K,[43,44] which is attributed to impurity incorporation as a result of the fabrication process.[45] Moreover, a closer examination of the data in the inset of Figure 5d suggests that $R$ does not vary linearly with $T$ across the entire thermal regime examined. Liu et al.[43] used the Efros−Shklovskii model to calculate the activation energy $E_a$ over the entire $T$-range from 5 to 340 K,


DOI: 10.1021/acsami.9b00603
ACS Appl. Mater. Interfaces 2019, 11, 24349−24359

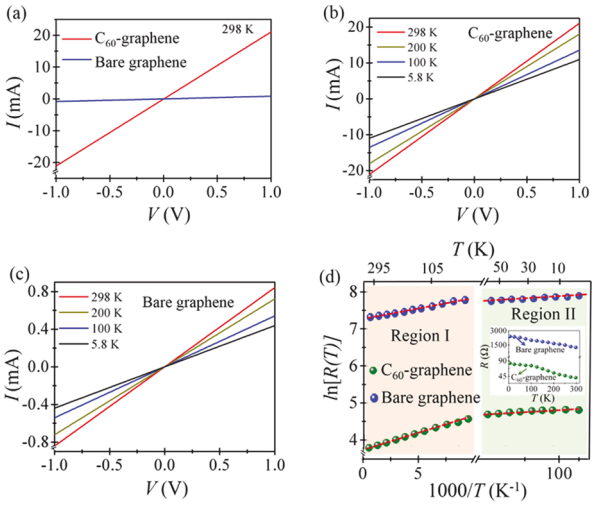


**Figure 5.** (a) $I-V$ of bare graphene and the $C_{60}$−graphene hybrid at 298 K, which shows the increased current levels in the latter. $I-V$ of (b) $C_{60}$−graphene and (c) bare graphene at different $T$'s. At $V \approx 1$ V, $I$ increases from ∼0.38 mA at ∼5.8 K to ∼0.8 mA at ∼298 K for bare graphene (c) and ∼9 mA at ∼5.8 K to ∼20 mA at ∼298 K for the $C_{60}$−graphene hybrid (b). (d) Logarithmic plot of $\ln[R(T)]$ as a function of $1000/T$, where the red lines show the linear fit of the data for the bare graphene (blue markers) and $C_{60}$−graphene (green markers) in the two regions, namely region I (∼65−298 K) and region II (∼5.8−60 K). The $R$ of the bare graphene and the hybrids decreases as $T$ increases, as shown in the inset. The $\ln[R(T)]$ data are fit to the Arrhenius function from which the fitting results yield $E_a$ values (from slope). The $E_a$ values are tabulated for region I and region II and the results are summarized in Table 2.

but the scatter in the data was significant. Here we explored two $T$-regimes, region I and region II, illustrated in Figure 5d, where the data are fit to the Arrhenius model[46] denoted by eq 1 below

$$R(T) = R_0 \exp\left[\frac{E_a}{2kT}\right] \quad (1)$$

where $R_0$ is the $R$ at $T = \infty$, and $k$ is the Boltzmann constant. Taking the logarithm of both sides of eq 1 yields

$$\ln R = \ln R_0 + \frac{E_a}{2kT} \quad (2)$$

where a linear relationship is expected between $\ln[R(T)]$ and $T$. From plots of $\ln[R(T)]$ versus $1000/T$ in Figure 5d, the $E_a$ values were extracted from the slope of the fit. Table 2 delineates the $E_a$ values in meV and the $r^2$ fitting parameters are shown, where $r$ is the correlation coefficient. Again, two different regions are noted, where region I refers to $T$ from ∼65 to 298 K and region II covers $T$ from ∼5.8 to 60 K for both bare graphene and the $C_{60}$−graphene hybrid, as shown in Figure 5d and Table 2. From the nonzero $E_a$ values, a thermally activated conduction mechanism appears to govern charge carrier transport in the devices where $R$ and $T$ are inversely related. For the higher $T$-regime, region I, the $E_a$ (region I) < $E_a$ (region II) for both the bare graphene and the hybrids. The thermal generation of the carriers at higher $T$ results in more of the carriers overcoming the existing built-in potential given the lower $E_a$ of ∼0.73 meV (region I). In the lower $T$ regime (region II), the kinetic energy of the carriers decreases, hindering their ability to overcome the existing built-in potential barrier, which increases $E_a \approx 0.94$ meV. Thus, the

**Table 2. Activation Energy $E_a$ and Correlation Coefficient $r^2$ Fitting Values for Bare Graphene and the $C_{60}$−Graphene Hybrid for Region I (∼65−298 K) and Region II (∼5.8−60 K)[a]**

| | region I (∼65−298 K) | | region II (∼5.8−60 K) | |
|---|---|---|---|---|
| device | $E_a$ (meV) | $r^2$ | $E_a$ (meV) | $r^2$ |
| bare graphene | ∼0.73 | ∼0.915 | ∼0.94 | ∼0.994 |
| $C_{60}$−graphene | ∼0.34 | ∼0.926 | ∼0.81 | ∼0.993 |

[a]The $E_a$ for the hybrid is lower in both regions compared to graphene, driven largely by the increased carrier concentration from doping. Additionally, the $E_a$ (region I) < $E_a$ (region II) for both the hybrid and bare graphene given the higher kinetic energies available for the carriers at higher $T$ (region I) to overcome the potential barrier at the interface.

$E_a$ values for both regions I and II for the hybrid structures are lower, ∼0.34 and ∼0.81 meV, respectively, relative to bare graphene. Given that an Ohmic response is seen from the $I-V$s in Figure 5a, we suspect minimal tunneling effects to arise at room temperature, because a suppressed conductance region would be evident at low voltages if tunneling were dominant, which was not observed even at low temperatures. Additionally, clean, residue-free viscoelastic stamping was used to transfer graphene flakes onto the Mo contacts which minimized contaminants at the interface. The absence of the $D$-peak (at ∼1350 $cm^{-1}$) for the $C_{60}$−graphene hybrid in the Raman spectra given by the red-colored plot in Figure 3a suggests that the likelihood of charged impurity residues from the electrophoretic deposition process is minimal. Moreover, through electronic transport measurements at low temperatures below about ∼15 or ∼20 K, the amplitude of the thermally driven phonon vibrations is significantly reduced, and impurity scattering becomes dominant, where the latter is temperature independent. Thus, if impurity scattering were dominant, this would likely have reflected itself through a temperature-independent $R-T$ characteristic at low temperatures where the slope of the line in the Figure 5d inset would be essentially zero for $C_{60}$−graphene for a $T$ below 15 or 20 K. Because the slope is nonzero and similar in character to the other thermal regimes, we deduce through such transport measurements, the charged impurities are likely to be low in concentration and appear to not impact the properties of the hybrids, which is also consistent with the absence of the $D$-band in the Raman spectra.

Next, optoelectronic measurements of the devices were initiated by exposing the hybrids to a white light source, as shown by the data in Figure 6a, where an incoming light power density ∼3 mW/$cm^2$ was used under vacuum conditions at room $T$. The photocurrent $I_{ph}$ behavior and the $\mathcal{R}$ of the hybrid structure was studied, which are key figures of merit for a gauging photodetector response. The $I_{ph}$ is defined as the difference between the current under exposure to light $I_{light}$ and the dark current ($I_{dark}$), where $I_{ph} = I_{light} - I_{dark}$. A photoresponse was not detectable in our bare graphene devices with the available instrumentation, as the $I_{ph}$ measured was below the picoamp range. As reported earlier, in graphene the short photon-generated carrier lifetimes on the scale of picoseconds likely comes into play, and the on−off ratio is also rather poor.[47] On the other hand, the hybrid devices show an excellent modulation of the $I_{ph}$ with the incoming on−off white light pulses, where $I_{ph}$ rose above 7 mA, as shown in Figure 6a.


DOI: 10.1021/acsami.9b00603
ACS Appl. Mater. Interfaces 2019, 11, 24349−24359

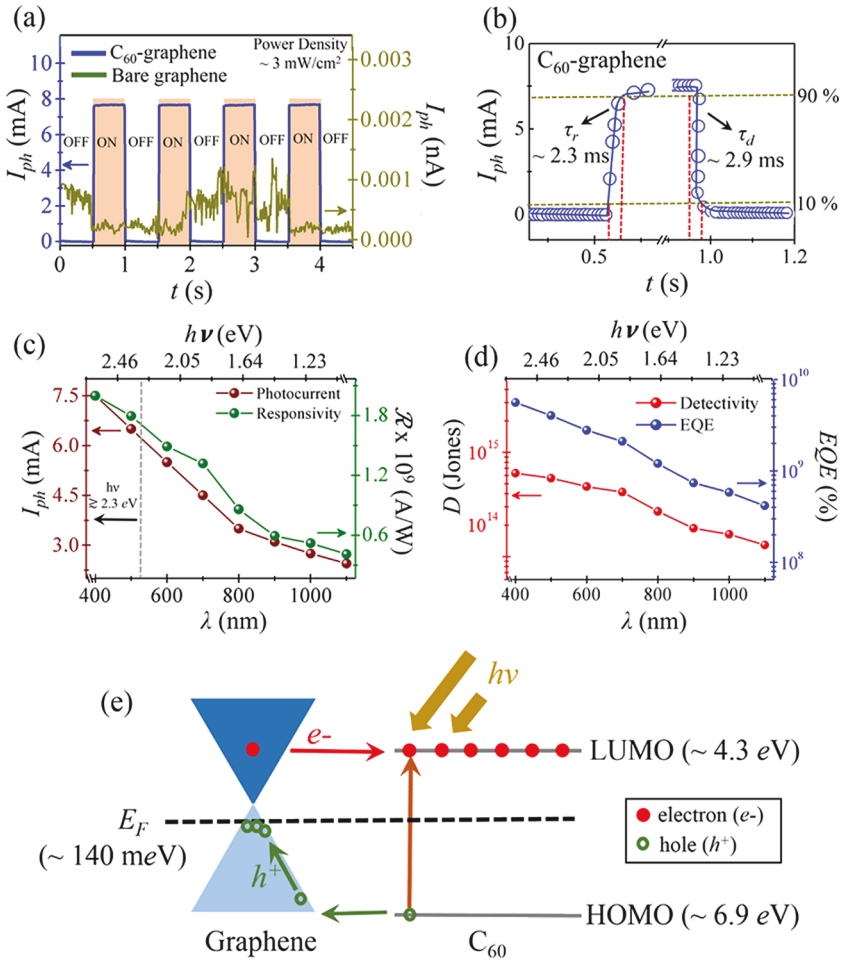


**Figure 6.** (a) $I_{ph}$ of bare graphene and the $C_{60}$−graphene hybrid as a function of $t$, where the former shows a negligible photoresponse (below pA), while the hybrids exhibit a substantial $I_{ph}$ > 7 mA for on−off white light pulses irradiated onto the device. (b) The $\tau_r \approx 2.3$ ms of the hybrid photodetector measured from ∼10 to ∼90% of the signal peak value, and $\tau_d \approx 2.9$ ms from ∼90 to ∼10% of the signal peak value at ∼1 V under vacuum, 298 K and a power density of ∼3 mW/cm$^2$. The $\mathcal{R}$ measured for the white light source of the hybrid was ∼$2 \times 10^9$ A/W. (c) $I_{ph}$ and $\mathcal{R}$ of $C_{60}$−graphene as a function of $\lambda$. $I_{ph}$ and $\mathcal{R}$ decrease from ∼7.5 to ∼2.9 mA and ∼$1.9 \times 10^9$ to ∼$4 \times 10^8$ A/W, respectively, for $\lambda \approx 400$−1100 nm using a tunable laser source. (d) $D$ and EQE of $C_{60}$−graphene as a function of $\lambda$ at room $T$. At a $\lambda \approx 400$ nm laser source, the device shows high $D$ ≈ $10^{15}$ jones and high EQE ≈ $10^9$% which decreased to ∼$10^{14}$ jones and ∼$10^8$% at $\lambda \approx 1100$ nm. (e) Band diagram of our $C_{60}$−graphene hybrid showing the photoexcited charge transfer and electron trapping processes and the subsequent downward shift in $E_F$ by ∼140 meV because of hole doping based on the Raman data.

From the multiple white light pulses, the response time of the photodetector was also measured, with the magnified profile of a single pulse in Figure 6b. From this, the rise time $\tau_r$ was measured from ∼10% of the noise floor in the off-state or minimum current to ∼90% of the signal peak value; similarly, the decay time $\tau_d$ was computed from ∼90 to ∼10% of the maximum and minimum signal intensities, respectively. The $\tau_r$ and $\tau_d$ of the hybrid structure were computed to be ∼2.3 and ∼2.9 ms, respectively. The response times, $\tau_r$ and $\tau_d$, computed here suggest that the $C_{60}$−graphene hybrids are much faster compared to other graphene hybrid photodetectors reported previously, such as GaN−graphene and perovskite−graphene structures, whose response times are >100× slower.[13,14] Ojeda-Aristizabal et al.[17] have conducted an in-depth study of the $C_{60}$−graphene hybrid on h-BN, where the transport was measured using a three-terminal photogating device configuration (gate voltage applied), which is unlike our two-terminal photoconductive device configuration where no gate voltage was applied. It is also important to note that in our experiments, we used the electrophoretic deposition technique to deposit the $C_{60}$ molecules. Interestingly, Ojeda-Aristizabal et al.,[17] notes that for $C_{60}$−graphene deposited directly on an $SiO_2$ substrate using thermal evaporation (in Supporting Information section of ref 17, pg 6), where thermal steps are involved, a change in doping in graphene is observed due to parasitic charges on the substrate, impeding the use of such samples for the quantifying charge transfer between graphene and crystalline $C_{60}$. Thus, keeping this in mind, we used the electrophoretic deposition technique which is carried out at room temperature and avoids thermal steps. The $\mathcal{R}$ of the hybrids was also calculated using $\mathcal{R} = \frac{I_{ph}}{P}$ where $\mathcal{R} \approx 2 \times 10^9$ A/W for the hybrid at ∼1 V and $P \approx 3.3$ pW with the incoming white light source. These values are ∼10 times higher compared to $\mathcal{R}$ values of other graphene-based photodetectors reported previously.[15,17,47−49] The high $\mathcal{R}$ values of the hybrid are attributed to the effective separation of the photogenerated electron−hole pairs at the hybrid interface, and the photogenerated holes transferred into graphene recirculating many times to yield a high photoconductive


DOI: 10.1021/acsami.9b00603
ACS Appl. Mater. Interfaces 2019, 11, 24349−24359

**Table 3. Limited Prior Work Has Been Conducted on Photodetectors Based on Hybrids Derived from Multilayer Graphene (MLG) Which is the Focus of Our Study, While Single Layer Graphene (SLG) and Bilayer Graphene (BLG) are More Extensively Studied, As Shown below**

| bare graphene | hybrid | detector type | $\lambda$ (nm) | bias (V) | $\mathcal{R}$ at $RT$ (A/W) | $D$ (jones), EQE (%) | refs |
|---|---|---|---|---|---|---|---|
| SLG | PbS QDs | photogating/photoconductive | white light | ~0.001 | ~$2.8 \times 10^5$ | | 49 |
| SLG, BLG | PbS QDs | photogating | ~532, 1050, and 1600 | ~5 | ~$5 \times 10^7$ | $D \approx 7 \times 10^{13}$ | 15 |
| SLG | few-layer $MoS_2$ | photogating/photoconductive | ~635 | ~0.1 | ~$5 \times 10^8$ | | 47 |
| SLG | ZnO QDs | photogating | ~325, 445 | ~0.001 | ~$10^7$ | | 51 |
| BLG | metal−graphene−metal | photogating | ~1550 | ~10−60 | ~6.1 | EQE ≈ 50 | 48 |
| SLG | $MAPbI_3$ | photogating | ~450−750 | ~10 | ~$1.73 \times 10^7$ | $D \approx 2 \times 10^{15}$, EQE ≈ $10^8$ | 14 |
| SLG | $C_{60}$ | photogating | ~200 | ~0.25 | ~$10^7$ | EQE ≈ $10^8$ | 18 |
| **MLG** | **$C_{60}$** | **photoconductive** | **white light** | **~1** | **~$2 \times 10^9$** | **$D \approx 5.1 \times 10^{15}$** | **this work** |
| **MLG** | **$C_{60}$** | **photoconductive** | **~400** | **~1** | **~$1.9 \times 10^9$** | **$D \approx 4.5 \times 10^{15}$, EQE ≈ $10^9$** | **this work** |

gain.[14] This implies that the photoresponse is mainly dominated by $C_{60}$ molecules near the hybrid interface.[18]

The evolution of $I_{ph}$ was further characterized as a function of $\lambda$ using a tunable laser source where $\lambda$ was varied from ~400−1100 nm with the device biased at $V \approx 1$ V in vacuum and at room $T$. As $\lambda$ is increased from ~400 to 1100 nm, the $I_{ph}$ decreased from ~7.5 to ~2.9 mA and the $\mathcal{R}$ also decreased from ~$1.9 \times 10^9$ to ~$4 \times 10^8$ A/W, as seen in Figure 6c. This decrease is likely due to the transport gap ($E_t$) of crystalline $C_{60}$, which is believed to be ~2.3−2.4 eV. Free photocarriers are generated when the photon energy ($h\nu$) is considerably higher than ~2.3−2.4 eV where the highly excited excitons (hot excitons) in $C_{60}$ dissociate.[50]

Other important figures of merit for photodetectors are $D$ and EQE. These are calculated using $D\ (\text{jones}) = \mathcal{R}\left(\frac{\sqrt{A}}{\sqrt{2 \cdot e \cdot I_{dark}}}\right)$ and $\text{EQE}\ (\%) = \left(\frac{hc}{e \cdot \lambda}\right)\mathcal{R}$, where $e$ is the electronic charge in Coulombs and $A$ is the active area of the photodetector in $\mu m^2$.[31] From this, the device was calculated to have a high $D$ of ~$10^{15}$ jones and a high EQE of ~$10^9$% at $\lambda \approx 400$ nm, which decreased to ~$10^{14}$ jones and ~$10^8$%, respectively, at $\lambda \approx 1100$ nm, as shown in Figure 6d. The value for $D$ and EQE are comparable to previously reported values for graphene−perovskite devices ($D \approx 0^{15}$ jones and EQE ≈ $10^8$%).[14] We believe that the high gain of the hybrid device originates from the continuous hole-doping in graphene. The holes in graphene move efficiently and are largely unperturbed, and can circulate multiple times through the circuit, giving a large $I_{ph}$.[47] The device performance of our $C_{60}$−graphene-based photodetector devices formed using the electrophoretic deposition technique is summarized in Table 3 and compared with other graphene-based hybrids reported previously,[14,15,18,47−49,51] from which the exceptional figures of merit of our hybrid devices are easily evident.

We also postulate a band diagram to explain the mechanism of the observed photoresponse, as shown schematically in Figure 6e. The $E_F$ of pristine graphene is located at the $K$ point of the Brillouin zone, where valence and conduction bands meet at the Dirac point. The LUMO and highest occupied molecular orbital of $C_{60}$ are ~4.3 and ~6.9 eV.[52] Graphene serves as a high-mobility charge transport channel, and charge transfer occurs at the $C_{60}$−graphene interface because of which a built-in field is established at the interface of the hybrid.[14] Upon illumination, $C_{60}$ absorbs photons with $h\nu \gtrsim 2.3$ eV.[50] The photoinduced carriers in graphene are then separated and transferred by the built-in field of the $C_{60}$−graphene hybrid interface. Because $C_{60}$ is an electron-acceptor, holes are driven into graphene and the hole population increases,[16] which leads to a downward shift in $E_F$ within graphene,[53] while electrons are injected into $C_{60}$ and charge neutrality is maintained. Also, Bautista-Flores et al.[54] reported that hole doping in exfoliated graphene shifts $E_F$ through various process treatments, where $E_F$ and carrier concentration ($n$) at room $T$ were calculated from the Raman data using eqs 3 and 4 below

$$E_F\ (\text{eV}) = \left|\frac{\text{position (G-band)} - 1580}{42}\right| \tag{3}$$

$$n\ (\text{cm}^{-2}) = \frac{(E_F/\hbar\nu_F)^2}{\pi} \tag{4}$$

Here, position (G-band) is 1586 $cm^{-1}$ of the hybrid in Figure 3b, $\nu_F$ is the Fermi velocity, and $\hbar$ is the modified Planck's constant (i.e., $\hbar = h/2\pi$, where $h = 6.626 \times 10^{-34}$ J s). From our Raman data at ~298 K in Figure 3b, the calculated value for $E_F \approx 140$ meV and $n$ accordingly were tabulated to be ~$1.19 \times 10^{12}$ $cm^{-2}$. It is interesting to note that Jnawali et al.[16] deduced a shift in $|E_F|$ by ~360 meV, even higher than the energy shift we observed with $|E_F| \approx 140$ meV. However, the shift in $E_F$ is in contrast to the values reported by Ojeda-Aristizabal et al.[17] The results are consistent with the observed $\Delta\omega^{(+)}$ shift in the G-band, which is due to hole doping in graphene and induces the downward shift in $E_F$ for graphene.[40] This is also consistent with the reduction in $I_{2D}/I_G$ by >60% in the hybrid compared to bare graphene at ~298 K as discussed earlier, consistent with hole doping[40] in graphene.

## 3. CONCLUSIONS

In conclusion, we have fabricated $C_{60}$−graphene hybrid devices by depositing $C_{60}$ using an electrophoretic deposition technique and measured the optoelectronic properties of the devices. Raman spectroscopy confirms electron transfer processes occurring from graphene to $C_{60}$ which results in a low shift in $E_F$ of graphene by ~140 meV, thereby inducing hole doping in graphene. The optoelectronic measurements show that the clusters of $C_{60}$ on top of graphene cause photogenerated electron−hole pairs to separate at the interface and recirculate many times to yield a high photoconductive


DOI: 10.1021/acsami.9b00603
ACS Appl. Mater. Interfaces 2019, 11, 24349−24359

gain. The $\tau_r$ and $\tau_d$ of the hybrid structure were computed to be ~2.3 and ~2.9 ms, and this suggests that the $C_{60}$−graphene hybrid photodetectors are much faster than other graphene-based hybrids. The $\mathcal{R} \approx 10^9$ A/W was ~10 times higher compared to previously reported hybrids, while the $D$ was computed to be $\sim 10^{15}$ jones at $\lambda \approx 400$ nm at room $T$. To the best of our knowledge, our results represent the first approach towards the fabrication of $C_{60}$−graphene-based photodetectors using an electrophoretic deposition technique that does not rely on complicated fabrication processes and yields the highest reported values for photodetector device figures of merit.

## 4. METHODS

**4.1. Materials.** Highly oriented pyrolytic graphite crystal was obtained from SPI Supplies Grade SPI-1, which had dimensions of 10 × 10 × 1 mm. This crystal was taken and placed gently on residue-free blue medium tack-tape from Semiconductor Equipment Corp. Another piece of the tape was then taken and gently laid on the first tape to ensure adequate adhesion and was subsequently pulled apart. This step was repeated 3−4 times for the successful isolation of graphene. During exfoliation, it is important to keep good tension on the tape to avoid fragmentation of the graphene membranes. Various concentrations of $C_{60}$ (Sigma-Aldrich, product number: 572500) were prepared in a mixed solvent by adding acetonitrile and toluene in a ratio of 3:1 (v/v).

**4.2. Device Fabrication.** The devices were fabricated using standard photolithography for the metal contact pattering on $SiO_2$/Si substrates. Approximately ~100 nm of Mo was deposited using sputtering at ~200 W and ~3 mTorr Ar pressure which served as the contact electrode, followed by a metal lift-off process. It is believed that the temperature rise at our sample during sputtering used was below ~100 °C because the lift-off process proceeded smoothly and the sputtering power used did not cause the photoresist to cross-link. A viscoelastic stamping method was then used to transfer the graphene membrane onto the electrode. The procedure followed was the same as that described by Saenz et al.[31] It is believed that the temperature rise at our sample during sputtering used was below ~100 °C because the lift-off process proceeded smoothly and the sputtering power used did not cause the photoresist to cross-link. A Karl Suss MJB-3 mask aligner was used for the alignment and subsequent transfer. The $SiO_2$/Si substrate with the Mo electrodes was held on the wafer chuck. Meanwhile, graphene from blue tape was then attached to the poly-dimethylsiloxane gel-film, which adhered to a clear 4 in. × 4 in. glass plate mounted onto the mask aligner. The graphene membrane on the gel-film-glass plate assembly was then aligned to the Mo electrodes on the $SiO_2$/Si substrate using the mask aligner.

**4.3. Characterization.** Optical absorption spectroscopy was conducted using a CARY 5000 spectrophotometer in quartz cuvettes with ~0.3 mL volumetric capacity. For AFM, the images were acquired in the contact mode by an AFM Veeco microscope at ambient conditions (relative humidity ~30%) using a silicon tip with $k \approx 0.3$ N/m by Ted Pella Inc. The Raman data were obtained using a Horiba LabRAM HR Evolution, where the laser excitation $\lambda$ used was ~532 nm. The electronic and optoelectronic device characterization was conducted using a Lakeshore CRX-4K probe stage with $T$ control from ~5.8 to ~298 K, and a low noise semiconductor parameter analyzer, the Keysight B1500A. The photoresponse was measured at room $T$ by illuminating the device with a white light source (LEDR/4 type illuminator), which has a color $T \approx 6500$ K. The tunable spectral measurements were conducted using a tunable laser source, the Fianium LLFT Contrast from NKT Photonics. Both the broadband and narrowband sources were calibrated using the Thorlabs optical power meter PM100D.

## AUTHOR INFORMATION


### Corresponding Authors

*E-mail: anupama.kaul@unt.edu (A.B.K.).
*E-mail: echegoyen@utep.edu (L.E.).

### ORCID

Luis Echegoyen: 0000-0003-1107-9423
Anupama B. Kaul: 0000-0003-4052-8064


### Notes

The authors declare no competing financial interest.

## ACKNOWLEDGMENTS

We greatly appreciate the support received from the Air Force Office of Scientific Research (grant number FA9550-15-1-0200), the Army Research Office (grant number W911NF-15-1-0425), and the National Science Foundation (grant number NSF ECCS 1753933) that enabled us to pursue this work. A.B.K. is also grateful to the support received from the UNT start-up package for helping establish the Nanoscale Materials and Devices Laboratory and the PACCAR Endowed Professorship and Institute support. L.E. thanks the NSF for the generous support of this work under the grant (CHE-1801317) and to the NSF-PREM program (DMR-1205302). The Robert A. Welch Foundation is also gratefully acknowledged for an endowed chair to L.E. (grant AH-0033).

## REFERENCES


(1) Geim, A. K.; Novoselov, K. S. The Rise of Graphene. *Nat. Mater.* **2007**, *6*, 183−191.

(2) Ferrari, A. C.; Bonaccorso, F.; Fal'ko, V.; Novoselov, K. S.; Roche, S.; Bøggild, P.; Borini, S.; Koppens, F. H. L.; Palermo, V.; Pugno, N.; Garrido, J. A.; Sordan, R.; Bianco, A.; Ballerini, L.; Prato, M.; Lidorikis, E.; Kivioja, J.; Marinelli, C.; Ryhänen, T.; Morpurgo, A.; Coleman, J. N.; Nicolosi, V.; Colombo, L.; Fert, A.; Garcia-Hernandez, M.; Bachtold, A.; Schneider, G. F.; Guinea, F.; Dekker, C.; Barbone, M.; Sun, Z.; Galiotis, C.; Grigorenko, A. N.; Konstantatos, G.; Kis, A.; Katsnelson, M.; Vandersypen, L.; Loiseau, A.; Morandi, V.; Neumaier, D.; Treossi, E.; Pellegrini, V.; Polini, M.; Tredicucci, A.; Williams, G. M.; Hee Hong, B.; Ahn, J.-H.; Min Kim, J.; Zirath, H.; van Wees, B. J.; van der Zant, H.; Occhipinti, L.; Di Matteo, A.; Kinloch, I. A.; Seyller, T.; Quesnel, E.; Feng, X.; Teo, K.; Rupesinghe, N.; Hakonen, P.; Neil, S. R. T.; Tannock, Q.; Löfwander, T.; Kinaret, J. Science and Technology Roadmap for Graphene, Related Two-dimensional Crystals, and Hybrid Systems. *Nanoscale* **2015**, *7*, 4598−4810.

(3) Fadil, D.; Hossain, R. F.; Saenz, G. A.; Kaul, A. B. On the Chemically-assisted Excitonic Enhancement in Environmentally-friendly Solution Dispersions of Two-dimensional $MoS_2$ and $WS_2$. *J. Mater. Chem. C* **2017**, *5*, 5323−5333.

(4) Geim, A. K.; Grigorieva, I. V. Van der Waals Heterostructures. *Nature* **2013**, *499*, 419−425.

(5) Slavík, R.; Parmigiani, F.; Kakande, J.; Lundström, C.; Sjödin, M.; Andrekson, P. A.; Weerasuriya, R.; Sygletos, S.; Ellis, A. D.; Grüner-Nielsen, L.; Jakobsen, D.; Herstrøm, S.; Phelan, R.; O'Gorman, J.; Bogris, A.; Syvridis, D.; Dasgupta, S.; Petropoulos, P.; Richardson, D. J. All-optical Phase and Amplitude Regenerator for Next-generation Telecommunications Systems. *Nat. Photonics* **2010**, *4*, 690−695.

(6) Zhu, H.; Jiang, S.; Chen, H.; Roco, M. C. International Perspective on Nanotechnology Papers, Patents, and NSF awards (2000−2016). *J. Nanopart. Res.* **2017**, *19*, 370.

(7) Nair, R. R.; Blake, P.; Grigorenko, A. N.; Novoselov, K. S.; Booth, T. J.; Stauber, T.; Peres, N. M. R.; Geim, A. K. Fine Structure Constant Defines Visual Transparency of Graphene. *Science* **2008**, *320*, 1308.




DOI: 10.1021/acsami.9b00603
*ACS Appl. Mater. Interfaces* 2019, 11, 24349−24359

(8) Mak, K. F.; Ju, L.; Wang, F.; Heinz, T. F. Optical Spectroscopy of Graphene: From the Far Infrared to the Ultraviolet. *Solid State Commun.* **2012**, *152*, 1341−1349.
(9) Kaul, A. B. Two-dimensional Layered Materials: Structure, Properties, and Prospects for Device Applications. *J. Mater. Res.* **2014**, *29*, 348−361.
(10) Xia, F.; Mueller, T.; Golizadeh-Mojarad, R.; Freitag, M.; Lin, Y.-m.; Tsang, J.; Perebeinos, V.; Avouris, P. Photocurrent Imaging and Efficient Photon Detection in a Graphene Transistor. *Nano Lett.* **2009**, *9*, 1039−1044.
(11) Zhang, Y.; Tang, T.-T.; Girit, C.; Hao, Z.; Martin, M. C.; Zettl, A.; Crommie, M. F.; Shen, Y. R.; Wang, F. Direct Observation of a Widely Tunable Bandgap in Bilayer Graphene. *Nature* **2009**, *459*, 820−823.
(12) Hossain, R. F.; Deaguero, I. G.; Boland, T.; Kaul, A. B. Biocompatible, Large-format, Inkjet Printed Heterostructure $MoS_2$-graphene Photodetectors on Conformable Substrates. *npj 2D Mater. Appl.* **2017**, *1*, 28.
(13) Liu, C.-H.; Chang, Y.-C.; Norris, T. B.; Zhong, Z. Graphene Photodetectors with Ultra-broadband and High Responsivity at Room Temperature. *Nat. Nanotechnol.* **2014**, *9*, 273−278.
(14) Chang, P.-H.; Liu, S.-Y.; Lan, Y.-B.; Tsai, Y.-C.; You, X.-Q.; Li, C.-S.; Huang, K.-Y.; Chou, A.-S.; Cheng, T.-C.; Wang, J.-K.; Wu, C.-I. Ultrahigh Responsivity and Detectivity Graphene-perovskite Hybrid Phototransistors by Sequential Vapor Deposition. *Sci. Rep.* **2017**, *7*, 46281.
(15) Konstantatos, G.; Badioli, M.; Gaudreau, L.; Osmond, J.; Bernechea, M.; de Arquer, F. P. G.; Gatti, F.; Koppens, F. H. L. Hybrid graphene-quantum dot phototransistors with ultrahigh gain. *Nat. Nanotechnol.* **2012**, *7*, 363−368.
(16) Jnawali, G.; Rao, Y.; Beck, J. H.; Petrone, N.; Kymissis, I.; Hone, J.; Heinz, T. F. Observation of Ground and Excited State Charge Transfer at the $C_{60}$ /Graphene Interface. *ACS Nano* **2015**, *9*, 7175−7185.
(17) Ojeda-Aristizabal, C.; Santos, E. J. G.; Onishi, S.; Yan, A.; Rasool, H. I.; Lv, Y.; Zatzke, D. W.; Lin, C.-Y.; Watanabe, K.; Taniguchi, T.; Lanzara, A.; Zettl, A. Molecular Arrangement and Charge Transfer in $C_{60}$/Graphene Heterostructures. *ACS Nano* **2017**, *11*, 4686−4693.
(18) Qin, S.; Chen, X.; Du, Q.; Nie, Z.; Wang, X.; Lu, H.; Wang, X.; Liu, K.; Xu, Y.; Shi, Y.; Zhang, R.; Wang, F. Sensitive and Robust Ultraviolet Photodetector Array Based on Self-Assembled Graphene/C60 Hybrid Films. *ACS Appl. Mater. Interfaces* **2018**, *10*, 38326−38333.
(19) Correa, J.; Orellana, P.; Pacheco, M. Optoelectronic Properties of van der Waals Hybrid Structures: Fullerenes on Graphene Nanoribbons. *Nanomaterials* **2017**, *7*, 69.
(20) Santos, E. J. G.; Scullion, D.; Chu, X. S.; Li, D. O.; Guisinger, N. P.; Wang, Q. H. Rotational Superstructure in van der Waals Heterostructure of Self-assembled $C_{60}$ Monolayer on the $WSe_2$ Surface. *Nanoscale* **2017**, *9*, 13245−13256.
(21) Li, L. H.; Tian, T.; Cai, Q.; Shih, C.-H.; Santos, E. J. G. Asymmetric Electric Field Screening in van der Waals Heterostructures. *Nat. Commun.* **2018**, *9*, 1271.
(22) Lee, T. H.; Kim, K.; Kim, G.; Park, H. J.; Scullion, D.; Shaw, L.; Kim, M.-G.; Gu, X.; Bae, W.-G.; Santos, E. J. G.; Lee, Z.; Shin, H. S.; Nishi, Y.; Bao, Z. Chemical Vapor-Deposited Hexagonal Boron Nitride as a Scalable Template for High-Performance Organic Field-Effect Transistors. *Chem. Mater.* **2017**, *29*, 2341−2347.
(23) Pinkard, A.; Champsaur, A. M.; Roy, X. Molecular Clusters: Nanoscale Building Blocks for Solid-State Materials. *Acc. Chem. Res.* **2018**, *51*, 919−929.
(24) Yu, D.; Park, K.; Durstock, M.; Dai, L. Fullerene-grafted Graphene for Efficient Bulk Heterojunction Polymer Photovoltaic Devices. *J. Phys. Chem. Lett.* **2011**, *2*, 1113−1118.
(25) Ma, J.; Guo, Q.; Gao, H.-L.; Qin, X. Synthesis of $C_{60}$/Graphene Composite as Electrode in Supercapacitors. *Fullerenes, Nanotub. Carbon Nanostruct.* **2015**, *23*, 477−482.
(26) Zhang, K.; Zhang, Y.; Wang, S. Enhancing Thermoelectric Poperties of Organic Composites through Hierarchical Nanostructures. *Sci. Rep.* **2013**, *3*, 3448.
(27) Kim, K.; Lee, T. H.; Santos, E. J. G.; Jo, P. S.; Salleo, A.; Nishi, Y.; Bao, Z. Structural and Electrical Investigation of $C_{60}$−Graphene Vertical Heterostructures. *ACS Nano* **2015**, *9*, 5922−5928.
(28) Reveles, J. U.; Karle, N. N.; Baruah, T.; Zope, R. R. Electronic and Structural Properties of $C_{60}$ and $Sc_3N@C_{80}$ Supported on Graphene Nanoflakes. *J. Phys. Chem. C* **2016**, *120*, 26083−26092.
(29) Manna, A. K.; Pati, S. K. Computational Studies on Noncovalent Interactions of Carbon and Boron Fullerenes with Graphene. *ChemPhysChem* **2013**, *14*, 1844−1852.
(30) Nikzad, S.; Hoenk, M.; Jewell, A.; Hennessy, J.; Carver, A.; Jones, T.; Goodsall, T.; Hamden, E.; Suvarna, P.; Bulmer, J.; Shahedipour-Sandvik, F.; Charbon, E.; Padmanabhan, P.; Hancock, B.; Bell, L. Single Photon Counting UV Solar-blind Detectors using Silicon and III-nitride Materials. *Sensors* **2016**, *16*, 927.
(31) Saenz, G. A.; Karapetrov, G.; Curtis, J.; Kaul, A. B. Ultra-high Photoresponsivity in Suspended Metal-semiconductor-metal Mesoscopic Multilayer $MoS_2$ Broadband Detector from UV-to-IR with Low Schottky Barrier Contacts. *Sci. Rep.* **2018**, *8*, 1276.
(32) Kamat, P. V.; Barazzouk, S.; Thomas, K. G.; Hotchandani, S. Electrodeposition of $C_{60}$ Cluster Aggregates on Nanostructured $SnO_2$ Films for Enhanced Photocurrent Generation. *J. Phys. Chem. B* **2000**, *104*, 4014−4017.
(33) Xiong, P.-h.; Xiong, Y.; Chen, X.-y.; Chen, S.; Hou, S.-y.; Zhang, X.-b.; Liu, G.; Tian, Y.-c. The Photoresponse and Photoconductivity of Micron-sized $C_{60}$ Whiskers and Sub-millimeter-sized $C_{60}$ Clusterss. *Optoelectron. Lett.* **2014**, *10*, 47−50.
(34) Harigaya, K.; Abe, S. Optical-absorption Spectra in Fullerenes $C_{60}$ and $C_{70}$: Effects of Coulomb Interactions, Lattice Fluctuations, and Anisotropy. *Phys. Rev. B: Condens. Matter Mater. Phys.* **1994**, *49*, 16746−16752.
(35) Orlandi, G.; Negri, F. Electronic States and Transitions in $C_{60}$ and $C_{70}$ fullerenes. *Photochem. Photobiol. Sci.* **2002**, *1*, 289−308.
(36) Tian, S.; Yang, Y.; Liu, Z.; Wang, C.; Pan, R.; Gu, C.; Li, J. Temperature-dependent Raman Investigation on Suspended Graphene: Contribution from Thermal Expansion Coefficient Mismatch between Graphene and Substrate. *Carbon* **2016**, *104*, 27−32.
(37) Vizuete, M.; Barrejón, M.; Gómez-Escalonilla, M. J.; Langa, F. Endohedral and Exohedral Hybrids Involving Fullerenes and Carbon Nanotubes. *Nanoscale* **2012**, *4*, 4370−4381.
(38) Wang, W.; Peng, Q.; Dai, Y.; Qian, Z.; Liu, S. Temperature Dependence of Raman Spectra of Graphene on Copper Foil Substrate. *J. Mater. Sci.: Mater. Electron.* **2016**, *27*, 3888−3893.
(39) Calizo, I.; Balandin, A. A.; Bao, W.; Miao, F.; Lau, C. N. Temperature Dependence of the Raman Spectra of Graphene and Graphene Multilayers. *Nano Lett.* **2007**, *7*, 2645−2649.
(40) Casiraghi, C.; Pisana, S.; Novoselov, K. S.; Geim, A. K.; Ferrari, A. C. Raman Fingerprint of Charged Impurities in Graphene. *Appl. Phys. Lett.* **2007**, *91*, 233108.
(41) Fang, X.-Y.; Yu, X.-X.; Zheng, H.-M.; Jin, H.-B.; Wang, L.; Cao, M.-S. Temperature- and Thickness-dependent Electrical Conductivity of Few-layer Graphene and Graphene Nanosheets. *Phys. Lett. A* **2015**, *379*, 2245−2251.
(42) Feteira, A. Negative Temperature Coefficient Resistance (NTCR) Ceramic Thermistors: An Industrial Perspective. *J. Am. Ceram. Soc.* **2009**, *92*, 967−983.
(43) Liu, Y.; Liu, Z.; Lew, W.; Wang, Q. Temperature Dependence of the Electrical Transport Properties in Few-layer Graphene Interconnects. *Nanoscale Res. Lett.* **2013**, *8*, 335.
(44) Schiefele, J.; Sols, F.; Guinea, F. Temperature Dependence of the Conductivity of Graphene on Boron Nitride. *Phys. Rev. B: Condens. Matter Mater. Phys.* **2012**, *85*, 195420.
(45) Davaji, B.; Cho, H. D.; Malakoutian, M.; Lee, J.-K.; Panin, G.; Kang, T. W.; Lee, C. H. A Patterned Single Layer Graphene Resistance Temperature Sensor. *Sci. Rep.* **2017**, *7*, 8811.
(46) Michel, M.; Biswas, C.; Tiwary, C. S.; Saenz, G. A.; Hossain, R. F.; Ajayan, P.; Kaul, A. B. A Thermally-invariant, Additively


DOI: 10.1021/acsami.9b00603
*ACS Appl. Mater. Interfaces* 2019, 11, 24349−24359

Manufactured, High-power Graphene Resistor for Flexible Electronics. *2D Mater.* **2017**, *4*, 025076−025086.
(47) Roy, K.; Padmanabhan, M.; Goswami, S.; Sai, T. P.; Ramalingam, G.; Raghavan, S.; Ghosh, A. Graphene−$MoS_2$ Hybrid Structures for Multifunctional Photoresponsive Memory Devices. *Nat. Nanotechnol.* **2013**, *8*, 826−830.
(48) Mueller, T.; Xia, F.; Avouris, P. Graphene Photodetectors for High-speed Optical Communications. *Nat. Photonics* **2010**, *4*, 297−301.
(49) Zhang, D.; Gan, L.; Cao, Y.; Wang, Q.; Qi, L.; Guo, X. Understanding Charge Transfer at PbS-decorated Graphene Surfaces Toward a Tunable Photosensor. *Adv. Mater.* **2012**, *24*, 2715−2720.
(50) Kazaoui, S.; Minami, N.; Tanabe, Y.; Byrne, H. J.; Eilmes, A.; Petelenz, P. Comprehensive Analysis of Intermolecular Charge-transfer Excited States in $C_{60}$ and $C_{70}$ Films. *Phys. Rev. B: Condens. Matter Mater. Phys.* **1998**, *58*, 7689−7700.
(51) Guo, W.; Xu, S.; Wu, Z.; Wang, N.; Loy, M. M. T.; Du, S. Oxygen-assisted Charge Transfer between ZnO Quantum Dots and Graphene. *Small* **2013**, *9*, 3031−3036.
(52) Kang, S. J.; Yi, Y.; Kim, C. Y.; Cho, S. W.; Noh, M.; Jeong, K.; Whang, C. N. Energy Level Diagrams of $C_{60}$/Pentacene/Au and Pentacene/$C_{60}$/Au. *Synth. Met.* **2006**, *156*, 32−37.
(53) Das, A.; Pisana, S.; Chakraborty, B.; Saha, S. K.; Waghmare, U. V.; Yiang, K. S.; Krishnamurhthy, H. R.; Geim, A. K.; Ferrari, A. C.; Sood, A. K. Monitoring dopants by Raman scattering in an electrochemically top-gated graphene transistor. *Nat. Nanotechnol.* **2008**, *4*, 210−215.
(54) Bautista-Flores, C.; Sato-Berrú, R. Y.; Mendoza, D. Doping Graphene by Chemical Treatments Using Acid and Basic Substances. *J. Mater. Sci. Chem. Eng.* **2015**, *3*, 17−21.


DOI: 10.1021/acsami.9b00603
*ACS Appl. Mater. Interfaces* 2019, 11, 24349−24359